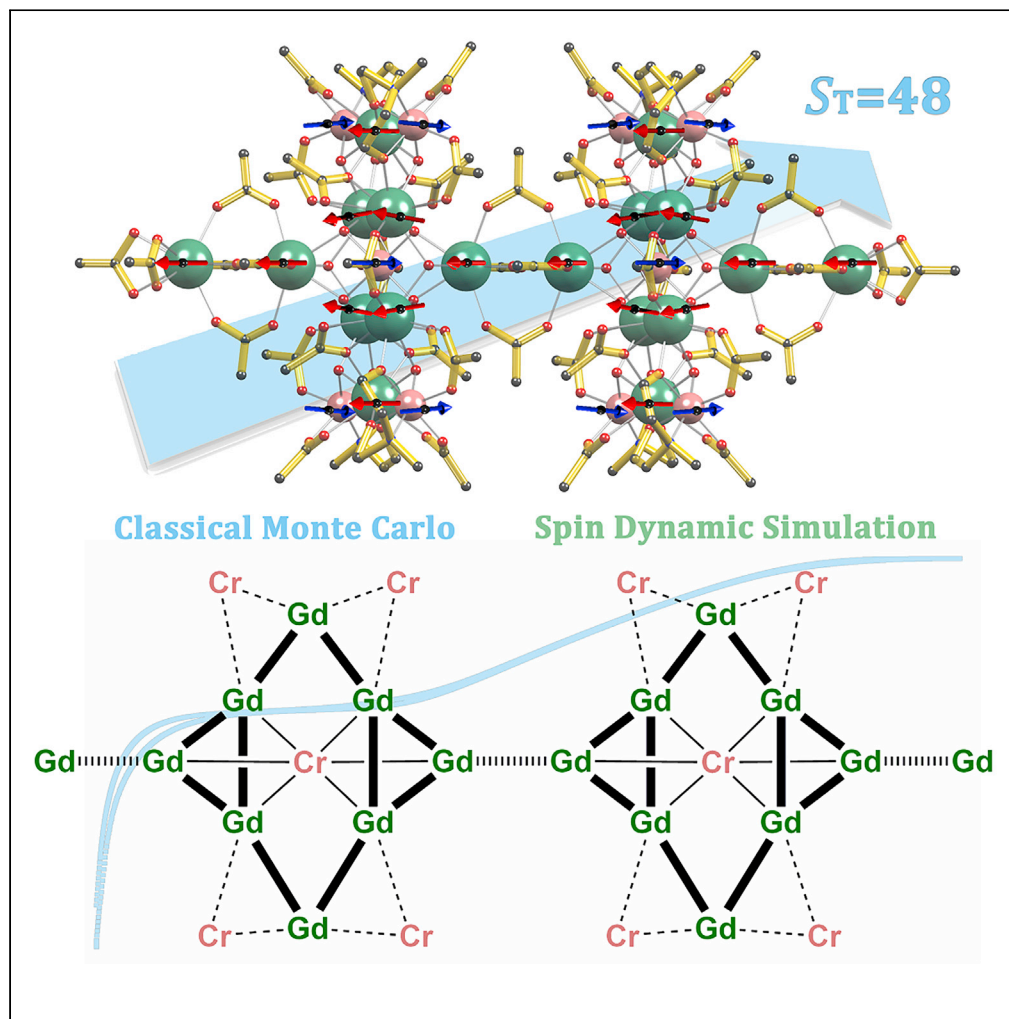


Article

A giant spin molecule with ninety-six parallel unpaired electrons



Lei Qin, Hao-Lan Zhang, Yuan-Qi Zhai, Hiroyuki Nojiri, Christian Schröder, Yan-Zhen Zheng

zheng.yanzhen@xjtu.edu.cn

Highlights

The largest $\{Cr_{10}RE_{18}\}$ molecular clusters were assembled for RE = Gd, Dy, and Y

The $\{Cr_{10}Gd_{18}\}$ cluster shows a large ground spin state of $S_T = 48$

The exchange coupling constants were determined by Classical Monte Carlo simulation

Spin dynamics simulation reveals a ferrimagnetic ground state of $\{Cr_{10}Gd_{18}\}$.

Qin et al., iScience 24, 102350
April 23, 2021 © 2021 The Author(s).
<https://doi.org/10.1016/j.isci.2021.102350>

Article

A giant spin molecule with ninety-six parallel unpaired electrons

Lei Qin,¹ Hao-Lan Zhang,¹ Yuan-Qi Zhai,¹ Hiroyuki Nojiri,² Christian Schröder,^{3,4} and Yan-Zhen Zheng^{1,5,*}

SUMMARY

Unpaired electrons which are essential for organic radicals and magnetic materials are hardly to align parallel, especially upon the increasing of spin numbers. Here, we show that the antiferromagnetic interaction in the largest Cr(III)-RE (rare earth) cluster $\{\text{Cr}_{10}\text{RE}_{18}\}$ leads to 96 parallel electrons, forming a ground spin state S_T of 48 for RE = Gd. This is so far the third largest ground spin state achieved in one molecule. Moreover, by using the classical Monte Carlo simulation, the exchange coupling constants J_{ij} can be determined. Spin dynamics simulation reveals that the strong Zeeman effects of 18 Gd(III) ions stabilize the ground ferrimagnetic state and hinder the magnetization reversals of these spins. In addition, the dysprosium(III) analog is an exchange-biasing single-molecule magnet. We believe that the ferrimagnetic approach and analytical protocol established in this work can be applied generally in constructing and analyzing giant spin molecules.

INTRODUCTION

Giant spin molecules which contain many parallel unpaired electrons can only be achieved using either organic radicals with p orbitals (Miller, et al., 1988; Fujita and Awaga, 1999; Rajca, 2002; Rajca et al., 2004a, 2004b; Phan, et al., 2019; Mendez-Vega, et al., 2019; Shu, et al., 2019) or coordination metal clusters with d or f orbitals (Stamatatos, et al., 2007; Manoli, et al., 2016; Abbasi et al., 2017; Morita et al., 2018; Alexandropoulos, et al., 2019; Kang, et al., 2015; Ako, et al., 2006; Charalambous, et al., 2012; Baskar, et al., 2010; Qin, et al., 2017; Baniodeh, et al., 2018; Chen, et al., 2018; Sánchez and Betley, 2018; Wang, et al., 2007). Though organic radicals can provide stronger magnetic interactions which even lead to the room temperature ferromagnetism (Fujita and Awaga, 1999), they are usually less stable due to the reactive highly delocalized electrons. In contrast, the unpaired electrons within the contracted d or f orbitals are much stable, but the magnetic interactions through superexchange coupling are much weaker. In addition to this disparity, large spin states require ferromagnetic coupling in both cases, which is, however, difficult to control due to the ubiquitous antiferromagnetic interactions.

Using this ferromagnetic strategy, the largest spin state for organic radicals is reported to be $S = 18$ (Rajca, 2002). However, it is difficult to achieve pure ferromagnetism in 3d transition metal clusters due to the orbital nature of 3d transition metal ions (Maniaki, et al., 2018; Langley et al., 2012). Successful examples include $\{\text{Fe}_{42}\}$ with $S = 45$ (Kang, et al., 2015), $\{\text{Mn}_{19}\}$ with $S = 83/2$ (Ako, et al., 2006), and other manganese-based cluster with S ranging from $51/2$ to $S = 61/2$ (Stamatatos, et al., 2007; Manoli, et al., 2016; Charalambous, et al., 2012; Wang, et al., 2007). Recently, high spin 3d metal-based molecules can be also realized at room temperatures (Sánchez and Betley, 2018). In contrast to 3d transition metals, rare-earth (RE) metal ions, e. g. Gd^{3+} with $s = 7/2$, can be also used to construct high spin molecules. Recent examples involve the $\{\text{Fe}_{10}\text{Gd}_{10}\}$ wheel with $S_T = 60$ (Baniodeh, et al., 2018) and the $\{\text{Ni}_{21}\text{Gd}_{20}\}$ cage with $S_T = 91$ (Chen, et al., 2018). Moreover, a ferrimagnetic measure has also led to a $\{\text{Cr}_8\text{Gd}_8\}$ wheel with $S_T = 16$ (Qin, et al., 2017).

Other than the synthetic difficulty, the physical understanding of such giant spin molecules is also challenging. Previous strategy to get insight of these molecules evolves almost exclusively the full diagonalization of massive matrix constructed by the exchange coupling-based spin Hamiltonian (Stamatatos, et al., 2007; Manoli, et al., 2016; Abbasi et al., 2017; Morita et al., 2018; Alexandropoulos, et al., 2019; Kang, et al., 2015; Ako, et al., 2006; Charalambous, et al., 2012; Baskar, et al., 2010; Qin, et al., 2017; Baniodeh, et al., 2018). However, this strategy is very time consuming and requires a lot of computing resources. For

¹Frontier Institute of Science and Technology (FIST), Xi'an Jiaotong University Shenzhen Research Academy, State Key Laboratory for Mechanical Behavior of Materials, MOE Key Laboratory for Nonequilibrium Synthesis of Condensed Matter, Xi'an Key Laboratory of Sustainable Energy and Materials Chemistry, School of Chemistry and School of Physics, Xi'an Jiaotong University, Xi'an 710054, China

²Institute of Materials Research (IMR), Tohoku University, Katahira, Sendai 980-8577, Japan

³Bielefeld Institute for Applied Materials Research, Bielefeld University of Applied Sciences, D-33619 Bielefeld, Germany

⁴Faculty of Physics, Bielefeld University, D-33615 Bielefeld, Germany

⁵Lead contact

*Correspondence: zheng.yanzhen@xjtu.edu.cn
<https://doi.org/10.1016/j.isci.2021.102350>



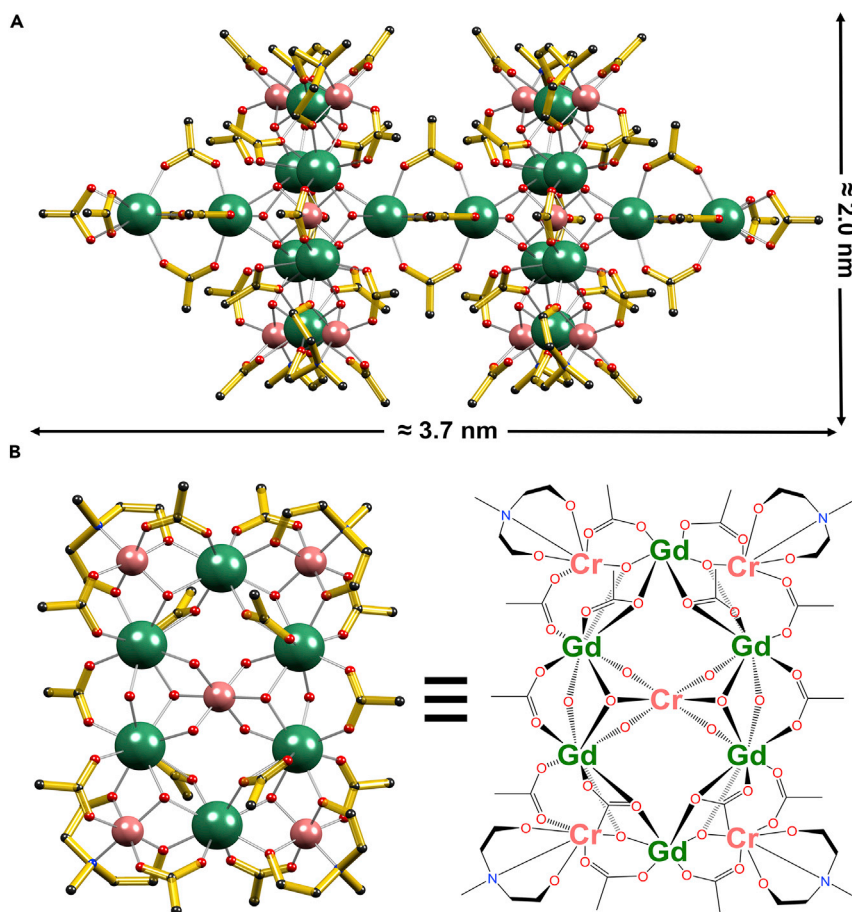


Figure 1. The structure analysis of 1-Gd

The molecular structure (A) and {Cr₅Gd₆} building moiety (B) of 1-Gd. Hydrogen atoms are omitted. Color codes: Cr, pink; Gd, sea green; C, gray; N, blue; O, red.

instance, the matrix dimension of the {Fe₁₀Gd₁₀} reaches $(2 \times 5/2 + 1)^{10} \times (2 \times 7/2 + 1)^{10} \approx 10^{17}$ and the {Ni₂₁Gd₂₀} cage reaches $(2 \times 1 + 1)^{21} \times (2 \times 7/2 + 1)^{20} \approx 10^{32}$. Typical modern computers cannot handle matrix dimensions larger than 10^8 , even with some approximations, the processing capacity only goes up to 10^9 , still far less than the demands of these systems.

Here, we further explore the Cr(III)-Gd(III) cages aiming at larger spin state and target a more rational assembling way (see below). The resulting octacosanuclear cages [Cr₁₀RE₁₈(mdea)₈(OH)₂₄(CH₃CO₂)₄₄·xCH₃CN·yH₂O (*abbr.* {Cr₁₀RE₁₈}; for RE = Gd, x = 3, y = 13, **1-Gd**; for RE = Dy, x = 6, y = 16, **1-Dy**; for RE = Y, x = 3, y = 11, **1-Y**; mdeaH₂ = *N*-methyl-diethanolamine) (Data S1–S6) are the largest Cr-RE mixed-metal coordination cluster up to date. The solvent amounts were determined using elemental analysis and thermogravimetric analysis; see the synthetic part in the supplemental information and Figures S1–S3. Classical Monte Carlo simulation using a Hamiltonian with dipole-dipole interaction reveals strong Zeeman effect induced by the Gd(III) ions, which leads to the a ferrimagnetic ground spin state ($S_T = 48$) and the slow flipping of the Gd(III) magnetic moments. Moreover, the Dy analog is a single-molecule magnet (SMM) with clearly exchange-biased feature in the hysteresis.

RESULTS AND DISCUSSION

The resulting {Cr₁₀RE₁₈} cages are shaped like a “dumbbell” if we view the {Cr₅RE₆} units as two “weights” and the three linear {RE₂} units as “bars” (see Figures 1, S4, and S5, demonstrated by 1-Gd). The two Gd(III) ions in {Gd₂} units are all bridged by four acetates in either $\mu\text{-}\eta^1\text{:}\eta^1$ or $\mu\text{-}\eta^2\text{:}\eta^1$ mode with the averaged Gd···Gd separation of 3.85 Å (Figure 1B) where the acetate anions were generated *in situ* by the

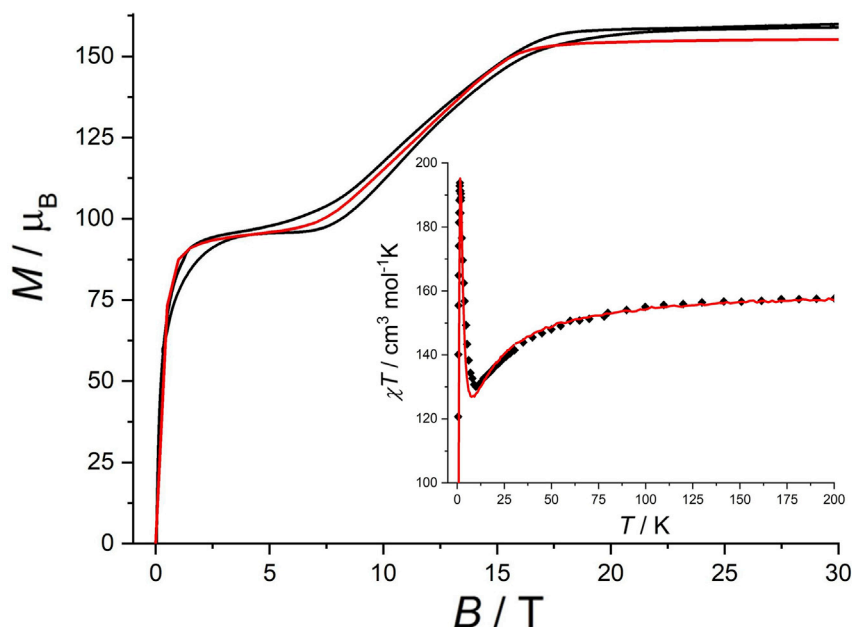


Figure 2. Pulsed-field magnetization at 0.4 K for 1-Gd

Inset: the $\chi T(T)$ plot for 1-Gd. Red lines in both panels: classical Monte Carlo simulation results using a four J model described in the text.

decomposition of acetoacetate (acac) or acetonitrile in the basic solvothermal synthetic conditions (Qin, et al., 2017). The outmost Gd(III) ions in the bilateral $\{Gd_2\}$ units of the molecule are further capped by two additional $\mu_3\text{-}\eta^1\text{:}\eta^1$ acetate anions, respectively. The other Gd(III) ions of the $\{Gd_2\}$ units are bridged by three $\mu_3\text{-OH}^-$ groups to other two Gd(III) ions and one Cr(III) ion in the $\{Cr_5Gd_6\}$ parts. The Gd(III) ions in the $\{Cr_5Gd_6\}$ moiety bridged by acetates and $\mu_3\text{-OH}^-$ groups form a distortedly capped hexagon circling one central Cr(III) ion and separating the other four corner Cr(III) ions. All the $Cr\cdots Gd$ separations are similar, ranging from 3.38 to 3.57 Å; and the $Gd\cdots Gd$ distances in the $\{Cr_5Gd_6\}$ part are slightly longer than those in the $\{Gd_2\}$ dimers, ranging from 3.88 to 4.23 Å. The crystallography information of three complexes is shown in Table S1, and the RE-O, Cr-O, RE-N, and Cr-O bond distances are listed in Tables S2–S4. The metal contents (Cr and RE) were also analyzed with inductively coupled plasma mass spectrometry, affording perfect agreements with the expected values (Table S5). The oxidation states of RE and Cr metal ions were also analyzed which confirm all of them are +3 valence (Table S6). For 3D packing, the molecules align parallelly, and the nearest $Cr\cdots Cr$, $Cr\cdots Gd$, and $Gd\cdots Gd$ distances of adjacent molecules are 8.07, 7.08, and 8.99 Å, respectively (Figure S5).

Direct current magnetic susceptibilities of 1-Gd, 1-Dy, and 1-Y (Figure S6) show that the χT products (in $\text{cm}^3 \text{mol}^{-1} \text{K}$) are in good agreement with the expected values for ten non-interacting Cr(III) and eighteen RE(III) ions (calculated by assuming $g_{Cr} = 2.0$ and $g_{Gd} = 2.0$, measured): for 1-Gd (160.5, 157.8); for 1-Dy (273.8, 273.2); and for 1-Y (18.8, 18.3). Upon cooling, 1-Gd and 1-Dy show typical ferrimagnetic behavior where the χT product decreases slowly down to a minimum at ca. 10 and 18 K, for 1-Gd and 1-Dy, respectively, before abruptly increasing. While for 1-Y, the χT product demonstrates Curie-type constant down to 25 K. The Curie-Weiss fitting gives the Curie constant (C) of $18.37 \text{ cm}^3 \text{mol}^{-1} \text{K}$ and Weiss constant (θ) of -0.06 K (Figure S7). The small Weiss constants indicate negligible magnetic interaction in 1-Y.

For 1-Gd, the two-step field-dependent magnetization is clearly shown (Figures 2 and S8): the first step is from 2 to 7 T with the value around $96(3) \mu_B$, which is in good agreement with the $S = 48$ spin state ($S = 7/2 \times 18 - 3/2 \times 10 = 48$; $M = gS = 96 \mu_B$ by assuming $g = 2.0$); the second step is from 17 to 30 T with the value of $156.0(3) \mu_B$, which is consistent to a full aligned spin state ($M = gS = g \times (7/2 \times 18 + 3/2 \times 10) = 156.0 \mu_B$ by assuming $g = 2.0$). The near linear increase from 8 to 14 T manifests the spin-flop behavior in 1-Gd. The small hysteresis effect between the up and down cycle originates from the competition between the thermal relaxation and the fast change of the pulsed magnetic field. Static magnetic field at 0.5 K shows no

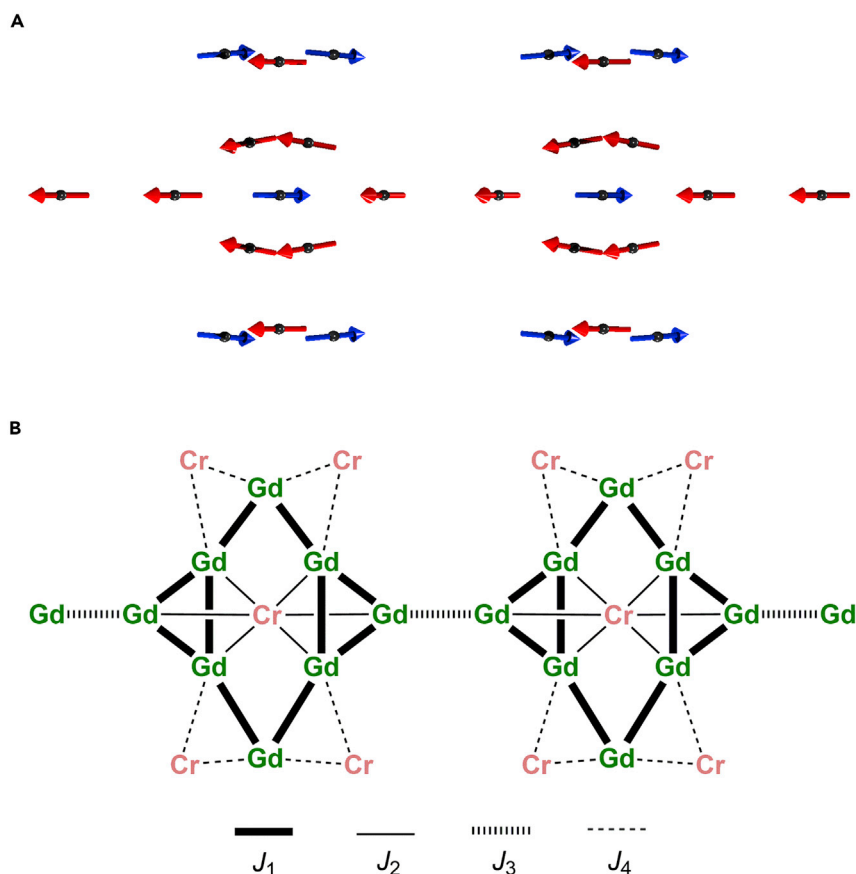


Figure 3. Ground spin state and magnetic exchange pathways of 1-Gd

(A) The initial spin state of 1-Gd at zero field.

(B) The proposed magnetic exchange pathways for 1-Gd.

hysteresis of 1-Gd (Figure S9), excluding the behavior of any long-range magnetic ordering introduced by the intermolecular interactions or dipole-dipole interactions.

The static magnetic properties of 1-Y were simulated using *PHI* software (Chilton, et al., 2013), yielding $J_{Cr \cdots Cr} = -0.07$ K and $g = 1.98$ (insert in the Figures S6 and S10), indicating very weak Cr \cdots Cr interactions. The absence of frequency-dependent behavior in alternating current (ac) susceptibility data of 1-Y also confirms this conclusion (Figure S11). The subtraction of the 1-Y data from 1-Gd and 1-Dy does not show obvious change in the shape of two plots, implying again the presence of ferrimagnetic phenomenon in both systems (Figure S12).

Thus, the exchange coupling interactions in 1-Gd can be simplified to four kinds (Figure 3), namely Gd \cdots Gd interaction within the {Cr₅Gd₈} units (J_1), Cr \cdots Gd interaction for the central Cr(III) ion and adjacent Gd(III) ions (J_2), Cr \cdots Gd interaction of four corner Cr ions and adjacent Gd(III) ions (J_4), and the Gd \cdots Gd interaction within the {Gd₂} dimers (J_3). If we use the regular matrix diagonal process, this evolves a Hilbert space dimension amounting to $(2 \times 3/2 + 1)^{10} \times (2 \times 7/2 + 1)^{18} \approx 10^{22}$, which is nearly impossible for an exact quantum mechanical treatment on common computer clusters. In order to simplify this process here, we use classical spin vectors \vec{S}_i (Engelhardt and Schröder, 2011). The Hamiltonian used for our simulations is given by Equation (1):

$$\hat{H} = -\frac{1}{2} \sum_{\substack{i,j \\ j \in n_n}}^N J_{ij}^c \vec{S}_i \vec{S}_j - \vec{B} \sum_i^N g_i \mu_B \vec{S}_i - \frac{\mu_0 \sum_{i,j}^N \mu_i \left(3 \left(\vec{S}_i \cdot \vec{e}_{ij} \right) \vec{e}_{ij} - \vec{S}_i \right) \vec{S}_j}{8\pi r_{ij}^3} \quad (\text{Equation 1})$$

Here, the first term describes the Heisenberg exchange interaction between two spins \vec{S}_i and \vec{S}_j via a classical exchange coupling constant J_{ij}^c . The second term defines the interaction of each spin with the external magnetic field \vec{B} where g_i is the Landé value which is chosen to be $g_i = 2$ for both Cr(III) and Gd(III) centers, therefore neglecting spin-orbit coupling. The third term describes the dipole-dipole interaction between spins which plays a significant role for very low temperatures due to the large magnetic moment per ion of the Gd(III) centers. In order to compare results obtained from Equation (1) with exact quantum results one has to normalize the spin vectors \vec{S}_i which leads to a scaling of the exchange constants such that $J_{ij}^c = J_{ij} S_i S_j$. Here, J_{ij} is the quantum exchange coupling constant and $S_i = f(s_i)$ is the magnitude of the spin vectors with s_i being the spin quantum number of the ion at site i , i.e. $s_i = 3/2$ for the Cr(III) centers and $s_i = 7/2$ for the Gd(III) centers. For $\frac{\mu_B B}{k_B T} \ll 1$, i.e., low magnetic fields and high temperatures, one uses $S_i = \sqrt{s_i(s_i + 1)}$ in accordance with Curie's law. However, for $\frac{\mu_B B}{k_B T} \gg 1$, i.e., high magnetic fields and low temperatures, one has to take $S_i = s_i$ which is the maximum z-component for the corresponding quantum spin in an external magnetic field. The determination of the exchange coupling constants J_{ij} has been done by performing Monte Carlo simulations (using $S_i = \sqrt{s_i(s_i + 1)}$) and fitting to the experimental $\chi T(T)$ data. The obtained exchange coupling constants were then used to calculate the $M(B)$ curves (using $S_i = s_i$) and we find excellent agreement (see Figure 2). The exchange interactions found were $J_1 = -0.13$ K, $J_2 = -1.43$ K, $J_3 = 0.63$ K, and $J_4 = -0.65$ K. The negative values of J_2 and J_4 confirm the dominated antiferromagnetic interaction between Cr(III) and Gd(III) ions.

Using the fitted exchange constants, we have calculated the ground spin state of **1-Gd** by solving the stochastic Landau-Lifshitz-Gilbert equation for $T \rightarrow 0$. The dipole-dipole interaction leads to the initial alignment of all spins roughly along the molecular axis (Figure 3). Furthermore, we have simulated the spin dynamics of our classical **1-Gd** model in an up and down ramping magnetic field at $T = 0$. With this type of simulation, one can nicely explain and visualize the main features of the measured $M(B)$ curve. In Figure S13, we present snapshots of the simulation for different values of the magnetic field. As soon as the external field is switched on, the Gd(III) ions align parallel to the external field, whereas the Cr(III) ions point into the opposite direction. Due to the strong Zeeman energy connected to the 18 Gd(III) ions, the system is stabilized by an exact ferrimagnetic state even for further increasing field values leading to the first plateau of the $M(B)$ curve. As soon as a certain critical field value is reached, first the 8 Cr(III) ions located at the corner start tilting and rotating toward the external field simultaneously. However, shortly after the two central Cr(III) ions start tilting and rotating simultaneously as well. This tilting and rotating increases the magnetization as shown in our $M(B)$ curve between 7 T and 18 T. Finally, all spins are aligned up in the field direction, and the system is saturated. We provide a video sequence in our supplemental material (see Video S1). It is important to note that the slope of the $M(B)$ curve between 7 T and 18 T depends on the rotation of the Gd ions only and specifically on the ratio of $J_2/J_4 = 2.2$. For values more or less than this, the slope changes significantly leading to strong deviations of our simulated finite temperature curve compared to the experimental data in Figure 2.

The magnetization of **1-Dy** at 2 K reaches $114.0 \mu_B$ without saturation up to 7 T (Figure S14). Ac susceptibility measurements at zero dc field show both temperature- and frequency-dependent in-phase (χ') and out-of-phase (χ'') signals (Figure S15) which suggests the presence of slow magnetic relaxation behavior in the **1-Dy**. Because of the magnetic anisotropy, the magnetic moment of the molecule tends to align in the "easy axis" direction. At finite temperature, it has a probability for the magnetization to flip "up" and "down" along the easy axis. The average time for this flip as a result of thermal fluctuation is called the relaxation time (τ). For the timescale of 0.001–1 s, the corresponding frequency of the ac susceptibility is 1000–1 Hz. By measuring the frequency-dependent ac susceptibility, the Cole-Cole plots of χ' versus χ'' can be obtained (Figure S16A), where the data were fitted using a generalized Debye model with α values ranging from 0.10 to 0.36, indicating a narrow distribution of relaxation times. Evaluated from variable frequency data (Table S7), the plot of $\ln(\tau)$ versus $1/T$ is extracted. The fitting of Arrhenius law $\tau = \tau_0 \exp(U_{\text{eff}}/k_B T)$ for the linear region gives $U_{\text{eff}} = 16(1)$ K and $\tau_0 = 5(3) \times 10^{-8}$ s (Figure S16B). Because the existence of quantum tunneling effect, the slow magnetic relaxation time is field dependent. With a small field (i.e. 200 Oe here), the quantum tunneling effect can be mitigated noted by the maxima of $\chi''(T)$ plots shifting to high frequencies (Figures S17 and S18). Because the relaxation is exponentially dependent upon cooling, at a certain temperature, the relaxation becomes very slow and the magnetization is "frozen". This temperature is called the "blocking temperature", T_B . Below T_B , the magnetization of **1-Dy** becomes hysteretic. Here, at 0.5 K, we observe a soft magnet type loop with a coercive field of 158 Oe (Figure 4). This is distinct to the usual "waist-restricted" hysteresis shape of Dy(III) SMMs, indicative of successful suppression of quantum

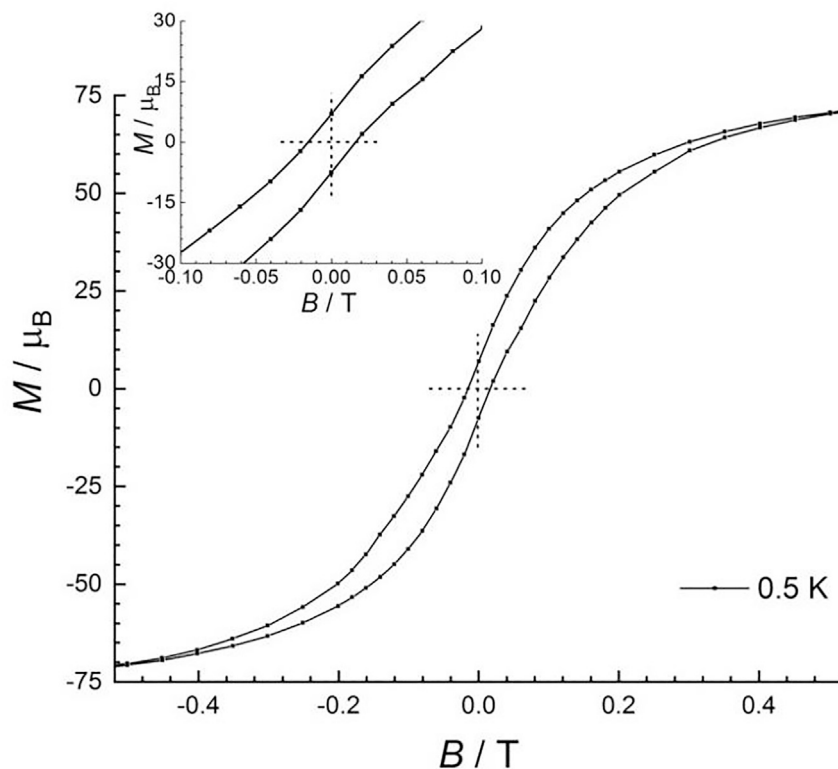


Figure 4. Magnetic hysteresis plots at 0.5 K for 1-Dy with a field sweep rate 6 Oe s^{-1}
The inset is the amplifying part at indicated field range.

tunneling of magnetization effect by exchange biasing (Langley, et al., 2013; Rinehart, et al., 2011; Morita et al., 2018; Kaemmerer, et al., 2020; Langley, et al., 2014). The absence of slow magnetic relaxation behavior on a diluted sample $1\text{-Y}_{0.95}\text{Dy}_{0.05}$ made by doping 5% Dy(III) ions into 1-Y unambiguously reveals that the slow magnetic relaxation behavior of 1-Dy comes from the molecule rather than the single ion anisotropy of the Dy(III) ions (Figures S19 and S20).

Conclusion

In summary, using the ferrimagnet strategy, the largest Cr(III)-RE(III) cluster with $S_T = 48$ is successfully assembled. From the case study of 1-Gd, we can see that the classical Monte Carlo method can handle arbitrarily large systems and complex interaction pathways, quickly obtaining numerically parameters for the classical Hamiltonian. Though the results lack the features of quantum mechanics, spin dynamic simulations can be used in visualizing the behavior of the microscopic magnetic moments and simulating dynamical equilibrium or non-equilibrium properties. We believe that such a synthetic strategy and analytical protocol can be used extensively for constructing and understanding giant spin molecules.

Limitations of the study

This work clearly shows that the antiferromagnetic interaction in the largest Cr(III)-RE cluster ($\text{Cr}_{10}\text{Gd}_{18}$) leads to 96 parallel electrons showing a ground spins state S_T of 48. Spin dynamics simulation reveals that the strong Zeeman effects of 18 Gd(III) ions stabilize the ground ferrimagnetic state. Additionally, it should be noted that this large ground spins state presents only at relatively lower temperatures. It remains to be improved in the future studies to maintain such large ground spins state at higher temperature range.

Resource availability

Lead contact

Further information and requests for resources should be directed to and will be fulfilled by the lead contact, Yan-Zhen Zheng (zheng.yanzhen@xjtu.edu.cn).

Materials availability

All unique reagents generated in this study are available from the lead contact upon reasonable request.

Data and code availability

The accession number for the crystallographic data reported in this paper is [Cambridge Crystallographic Data Center]: [1883413, 1883414 and 1883415].

METHODS

All methods can be found in the accompanying [transparent methods supplemental file](#).

SUPPLEMENTAL INFORMATION

Supplemental information can be found online at <https://doi.org/10.1016/j.isci.2021.102350>.

ACKNOWLEDGMENTS

This work was supported by the Shenzhen Science and Technology Program (JCYJ20180306170859634), National Natural Science Foundation of China (no. 21773130 and 21971203), State Key Laboratory for Mechanical Behavior of Materials (20182006), Key Laboratory Construction Program of Xi'an Municipal Bureau of Science and Technology (201805056ZD7CG40), Cyrus Chung Ying Tang Foundation, Fundamental Research Funds for the Central Universities, and the GIMRT (No. 18GK0005) program of the Institute for Materials Research (ICC-IMR, Sendai, Japan).

AUTHOR CONTRIBUTIONS

Y.-Z.Z. supervised the project. L.Q. carried out the experiments and most of the magnetic characterizations. L.Q. and H.-L.Z. performed the synthesis of the yttrium diluted sample. Y.-Q.Z. performed the magnetic data simulation of 1-Y using *PHI*. H.N. carried out the high-field magnetic measurements. C.S. performed the classical Monte Carlo and spin dynamic calculations. The manuscript was prepared by L.Q., H.N., C.S., and Z.Y.Z.

DECLARATION OF INTERESTS

The authors declare no competing interests.

Received: October 9, 2020

Revised: February 20, 2021

Accepted: March 18, 2021

Published: April 23, 2021

REFERENCES

- Abbasi, P., Quinn, K., Alexandropoulos, D.I., Damjanović, M., Wernsdorfer, W., Escuer, A., Mayans, J., Pilkington, M.T., and Stamatatos, C. (2017). Transition metal single-molecule magnets: a {Mn₃₁} nanosized cluster with a large energy barrier of ~60 K and magnetic hysteresis at ~5 K. *J. Am. Chem. Soc.* **139**, 15644–15647.
- Ako, A.M., Hewitt, I.J., Mereacre, V., Clérac, R., Wernsdorfer, W., Anson, C.E., and Powell, A.K. (2006). A ferromagnetically coupled Mn₁₉ aggregate with a record S=83/2 ground spin state. *Angew. Chem. Int. Ed.* **45**, 4926–4929.
- Alexandropoulos, D.I., Vignesh, K.R., Stamatatos, T.C., and Dunbar, K.R. (2019). Rare “Janus”-faced {Fe^{II}} single-molecule magnet exhibiting intramolecular ferromagnetic interactions. *Chem. Sci.* **10**, 1626–1633.
- Baniodeh, A., Magnani, N., Lan, Y., Buth, G., Anson, C.E., Richter, J., Affronte, M., Schnack, J., and Powell, A.K. (2018). High spin cycles: topping the spin record for a single molecule verging on quantum criticality. *npj Quant. Mater.* **3**, 10.
- Baskar, V., Gopal, K., Helliwell, M., Tuna, F., Wernsdorfer, W., and Winpenny, R.E.P. (2010). 3d-4f Clusters with large spin ground states and SMM behavior. *Dalton Trans.* **39**, 4747–4750.
- Charalambous, M., Moushi, E.E., Papatriantafyllopoulou, C., Wernsdorfer, W., Nastopoulos, V., Christou, G., and Tasiopoulos, A.J. (2012). A Mn₃₆Ni₄ ‘loop-of-loops-and-supertetrahedra’ aggregate possessing a high S_T = 26 ± 1 spin ground state. *Chem. Commun.* **48**, 5410–5412.
- Chen, W.-P., Singleton, J., Qin, L., Camón, A., Engelhardt, L., Luis, F., Winpenny, R.E.P., and Zheng, Y.-Z. (2018). Quantum Monte Carlo simulations of a giant [Ni₂₁Gd₂₀] cage with a S = 91 spin ground state. *Nat. Commun.* **9**, 2107.
- Chilton, N.F., Andersson, R.P., Turner, L.D., Soncini, A., and Murray, K.S. (2013). *PHI*: a powerful new program for the analysis of anisotropic monomeric and exchange-coupled polynuclear d- and f-block complexes. *J. Comput. Chem.* **34**, 1164–1175.
- Engelhardt, L., and Schröder, C. (2011). Simulating computationally complex magnetic molecules. In *Molecular Cluster Magnets*, R.E.P. Winpenny, ed. (World Scientific Publishers), pp. 245–296.
- Fujita, W., and Awaga, K. (1999). Room temperature magnetic bistability in organic radical crystals. *Science* **286**, 261–263.
- Kaemmerer, H., Baniodeh, A., Peng, Y., Moreno-Pineda, E., Schulze, M., Anson, C.E., Wernsdorfer, W., Schnack, J., and Powell, A.K. (2020). Inorganic approach to stabilizing nanoscale toroidicity in a tetraicosanuclear Fe₁₈Dy₆ single molecule magnet. *J. Am. Chem. Soc.* **142**, 14838–14842.

- Kang, S., Zheng, H., Liu, T., Hamachi, K., Kanegawa, S., Sugimoto, K., Shiota, Y., Hayami, S., Mito, M., Nakamura, T., et al. (2015). A ferromagnetically coupled Fe₄₂ cyanide-bridged nanocage. *Nat. Commun.* **6**, 5955.
- Langley, S.K., Chilton, N.F., Moubaraki, B., and Murray, K.S. (2012). Structure and magnetic exchange in heterometallic 3d–3d transition metal triethanolamine clusters. *Dalton Trans.* **41**, 1033–1046.
- Langley, S.K., Wielechowski, D.P., Vieru, V., Chilton, N.F., Moubaraki, B., Abrahams, B.F., Chibotaru, L.F., and Murray, K.S. (2013). A {Cr^{III}2Dy^{III}2} single-molecule magnet: enhancing the blocking temperature through 3d magnetic exchange. *Angew. Chem. Int. Ed.* **52**, 12014–12019.
- Langley, S.K., Wielechowski, D.P., Vieru, V., Chilton, N.F., Moubaraki, B., Chibotaru, L.F., and Murray, K.S. (2014). Modulation of slow magnetic relaxation by tuning magnetic exchange in {Cr₂Dy₂} single molecule magnets. *Chem. Sci.* **5**, 3246–3256.
- Maniaki, D., Pilichos, E., and Perlepes, S.P. (2018). Coordination clusters of 3d-metals that behave as single-molecule magnets (SMMs): synthetic routes and strategies. *Front. Chem.* **6**, 461.
- Manoli, M., Alexandrou, S., Pham, L., Lorusso, G., Wernsdorfer, W., Evangelisti, M., Christou, G., and Tasiopoulos, A.J. (2016). Magnetic “molecular oligomers” based on decametallc supertetrahedra: a giant Mn₄₉ cuboctahedron and its Mn₂₅Na₄ fragment. *Angew. Chem. Int. Ed.* **55**, 679–684.
- Mendez-Vega, E., Mieres-Perez, J., Chapyshev, S.V., and Sander, W. (2019). Persistent organic high-spin trinitrenes. *Angew. Chem. Int. Ed.* **58**, 12994–12998.
- Miller, J.S., Epstein, A.J., and Reiff, W.M. (1988). Molecular/organic ferromagnets. *Science* **240**, 40–47.
- Morita, T., Damjanović, M., Katoh, K., Kitagawa, Y., Yasuda, N., Lan, Y., Wernsdorfer, W., Breedlove, B.K., Enders, M., and Yamashita, M. (2018). Comparison of the magnetic anisotropy and spin relaxation phenomenon of dinuclear terbium(III) phthalocyaninato single-molecule magnets using the geometric spin arrangement. *J. Am. Chem. Soc.* **140**, 2995–3007.
- Phan, H., Heng, T.S., Wang, D., Li, X., Zeng, W., Ding, J., Loh, K.P., Wee, A.T.S., and Wu, J. (2019). Room-temperature magnets based on 1,3,5-triazine-linked porous organic radical frameworks. *Chem* **5**, 1223–1234.
- Qin, L., Singleton, J., Chen, W.-P., Nojiri, H., Engelhardt, L., Winpenny, R.E.P., and Zheng, Y.-Z. (2017). Quantum Monte Carlo simulations and high-field magnetization studies of antiferromagnetic interactions in a giant heterospin ring. *Angew. Chem. Int. Ed.* **56**, 16571–16574.
- Rajca, A. (2002). From high-spin organic molecules to organic polymers with magnetic ordering. *Chem. Eur. J.* **8**, 4834–4841.
- Rajca, A., Wongsriratanakul, J., Rajca, S., and Cerny, R.L. (2004a). Organic spin clusters: annelated macrocyclic polyarylmethyl polyradicals and a polymer with very high spin *S* = 6–18. *Chem. Eur. J.* **10**, 3144–3157.
- Rajca, A., Wongsriratanakul, J., and Rajca, S. (2004b). Organic spin clusters: macrocyclic-macrocyclic polyarylmethyl polyradicals with very high-spin *S* = 5–13. *J. Am. Chem. Soc.* **126**, 6608–6626.
- Rinehart, J.D., Fang, M., Evans, W.J., and Long, J.R. (2011). Strong exchange and magnetic blocking in N₂³⁻ radical-bridged lanthanide complexes. *Nat. Chem.* **3**, 538–542.
- Sánchez, R.H., and Betley, T.A. (2018). Thermally persistent high-spin ground states in octahedral iron clusters. *J. Am. Chem. Soc.* **140**, 16792–16806.
- Shu, C., Zhang, H., Olankitwanit, A., Rajca, S., and Rajca, A. (2019). High-spin diradical dication of chiral π-conjugated double helical molecule. *J. Am. Chem. Soc.* **141**, 17287–17294.
- Stamatatos, T.C., Abboud, K.A., Wernsdorfer, W., and Christou, G. (2007). “Spin Tweaking” of a high-spin molecule: an Mn₂₅ single-molecule magnet with an *S* = 61/2 ground state. *Angew. Chem. Int. Ed.* **46**, 884–888.
- Wang, W.-G., Zhou, A.-J., Zhang, W.-X., Tong, M.-L., Chen, X.-M., Nakano, M., Beedle, C.C., and Hendrickson, D.N. (2007). Giant heterometallic Cu₁₇Mn₂₈ cluster with *T_d* symmetry and high-spin ground state. *J. Am. Chem. Soc.* **129**, 1014–1015.

iScience, Volume 24

Supplemental information

A giant spin molecule

with ninety-six parallel unpaired electrons

Lei Qin, Hao-Lan Zhang, Yuan-Qi Zhai, Hiroyuki Nojiri, Christian Schröder, and Yan-Zhen Zheng

iScience, Volume ■ ■

Supplemental information

A giant spin molecule

with ninety-six parallel unpaired electrons

Lei Qin, Hao-Lan Zhang, Yuan-Qi Zhai, Hiroyuki Nojiri, Christian Schröder, and Yan-Zhen Zheng

Supplemental Tables

Table S1. Single crystal data and structure refinement for 1-RE (RE = Gd, Dy, and Y).

Related to Figure 1.

Compound	1-Gd	1-Dy	1-Y
Formula	C ₁₃₄ H ₂₇₉ N ₁₁ Cr ₁₀ ⁻ Gd ₁₈ O ₁₄₁	C ₁₄₀ H ₂₉₄ N ₁₄ Cr ₁₀ ⁻ Dy ₁₈ O ₁₄₄	C ₁₃₄ H ₂₇₅ N ₁₁ Cr ₁₀ ⁻ Y ₁₈ O ₁₃₉
<i>F</i> w (g mol ⁻¹)	7651.1	7922.8	6384.87
<i>T</i> (K)	296(2)	298(2)	298(2)
Crystal system	Monoclinic	Monoclinic	Monoclinic
Space group	<i>C</i> 2/ <i>m</i>	<i>C</i> 2/ <i>m</i>	<i>C</i> 2/ <i>m</i>
<i>a</i> (Å)	37.44(3)	37.899(12)	37.676(12)
<i>b</i> (Å)	22.51(3)	22.172(7)	21.951(7)
<i>c</i> (Å)	14.920(16)	14.947(5)	14.869(5)
α (deg.)	90	90	90
β (deg.)	92.55(2)	93.489(4)	93.417(4)
γ (deg.)	90	90	90
<i>V</i> (Å ³)	12565(26)	12536(7)	12275(7)
<i>Z</i>	2	2	2
<i>d</i> _{calc} (g cm ⁻³)	1.928	1.957	1.641
μ (mm ⁻¹)	5.175	5.790	4.711
Goof	1.034	1.049	1.017
<i>R</i> ₁ (>2 σ) ^a	0.0666	0.0636	0.0684
<i>wR</i> ₂ (all data) ^b	0.2227	0.2150	0.2216
No. CCDC	1883413	1883414	1883415

^a $R_1 = \sum ||F_o| - |F_c|| / \sum |F_o|$, ^b $wR_2 = [\sum w(F_o^2 - F_c^2)^2 / \sum w(F_o^2)^2]^{1/2}$

Table S2. Selected Bond Lengths for 1-Gd. Related to Figure 1.

Atom	Atom	Length/Å	Atom	Atom	Length/Å	Atom	Atom	Length/Å
Gd1	O2	2.312(11)	Gd3	O34	2.447(9)	Gd6	O27	2.440(19)
Gd1	O4	2.411(13)	Gd3	O35	2.382(12)	Gd6	O28 ¹	2.52(2)
Gd1	O5	2.419(12)	Gd4	O20	2.336(15)	Gd6	O28	2.52(2)
Gd1	O7	2.327(11)	Gd4	O22	2.439(10)	Gd6	O29	2.339(17)
Gd1	O12	2.467(11)	Gd4	O22 ¹	2.439(10)	Cr1	O1	1.951(11)
Gd1	O13	2.504(10)	Gd4	O23	2.352(16)	Cr1	O2	1.963(10)
Gd1	O14	2.506(10)	Gd4	O25	2.411(13)	Cr1	O3	2.025(12)
Gd1	O15	2.476(11)	Cr2	N2	2.120(18)	Cr1	O14	1.975(10)
Gd2	O1	2.382(12)	Cr3	O21	2.016(14)	Cr1	O17	1.993(11)
Gd2	O14	2.528(11)	Cr3	O22 ¹	2.009(10)	Cr1	N1	2.118(14)
Gd2	O15	2.670(11)	Cr3	O22	2.009(10)	Cr2	O6	2.034(14)
Gd2	O16	2.542(12)	Cr3	O31 ¹	1.990(10)	Cr2	O7	1.972(12)
Gd2	O18	2.465(11)	Cr3	O31	1.990(10)	Cr2	O8	1.941(14)
Gd2	O19	2.350(12)	Cr3	O32	2.024(14)	Cr2	O9	2.005(12)
Gd2	O20	2.479(9)	Gd5	O33	2.429(12)	Cr2	O13	1.981(11)
Gd2	O21	2.497(9)	Gd5	O34	2.334(15)	Gd4	O25 ¹	2.411(13)
Gd2	O22	2.480(10)	Gd5	O36 ²	2.586(15)	Gd4	O29	2.570(18)
Gd3	O8	2.325(12)	Gd5	O36	2.368(14)	Gd4	O30	2.423(17)
Gd3	O10	2.498(11)	Gd5	O37 ²	2.415(15)	Gd5	O31	2.422(10)
Gd3	O11	2.526(12)	Gd6	O23	2.631(18)	Gd5	O31 ¹	2.422(10)
Gd3	O12	2.649(11)	Gd6	O24	2.44(2)	Gd5	O33 ¹	2.429(12)
Gd3	O13	2.532(12)	Gd6	O26	2.411(15)			
Gd3	O31	2.488(10)	Gd6	O26 ¹	2.411(15)			
Gd3	O32	2.466(8)	Gd6	O27 ¹	2.440(19)			

¹+X,1-Y,+Z; ²1-X,1-Y,1-Z

Table S3. Selected Bond Lengths for 1-Dy. Related to Figure 1.

Atom	Atom	Length/Å	Atom	Atom	Length/Å	Atom	Atom	Length/Å
Dy1	O1 ¹	2.377(18)	Dy3	O10	2.464(8)	Dy6	O7	2.420(7)
Dy1	O1	2.377(18)	Dy3	O11	2.511(10)	Dy6	O8	2.433(8)
Dy1	O2 ¹	2.420(18)	Dy3	O12	2.655(9)	Dy6	O13	2.464(7)
Dy1	O2	2.420(18)	Dy3	O14	2.331(11)	Dy6	O25	2.693(10)
Dy1	O3	2.343(18)	Dy3	O15	2.296(11)	Dy6	O26	2.498(10)
Dy1	O5	2.394(15)	Dy3	O17	2.443(11)	Dy6	O28	2.333(10)
Dy1	O5 ¹	2.394(15)	Dy3	O19	2.424(8)	Dy6	O31	2.496(10)
Dy1	O35	2.700(18)	Dy3	O37	2.498(10)	Dy6	O33	2.419(10)
Dy1	O36	2.43(3)	Dy4	O10	2.378(9)	Dy6	O34	2.309(10)
Cr3	O27	1.952(10)	Dy4	O10 ¹	2.379(9)	Cr1	O8	2.000(9)
Cr3	O28	1.928(11)	Dy4	O19	2.303(13)	Cr1	O8 ¹	2.000(9)
Cr3	O30	2.010(11)	Dy4	O20 ²	2.367(13)	Cr1	O9	2.007(11)
Cr3	O31	1.972(10)	Dy4	O21 ²	2.592(13)	Cr1	O13	1.994(12)
Cr3	O32	1.971(10)	Dy4	O21	2.302(13)	Cr2	O15	1.923(12)
Cr3	N2	2.104(15)	Dy4	O22	2.365(10)	Cr2	O16	1.954(11)
Dy2	O3	2.505(17)	Dy4	O22 ¹	2.365(10)	Cr2	O18	1.989(11)
Dy2	O4	2.377(15)	Dy5	O12	2.429(10)	Cr2	O23	2.022(13)
Dy2	O6	2.371(12)	Dy5	O16	2.289(10)	Cr2	O37	1.970(9)
Dy2	O6 ¹	2.371(12)	Dy5	O24	2.363(12)	Cr2	N1	2.098(15)
Dy2	O7	2.303(12)	Dy5	O25	2.429(9)	Cr1	O10 ¹	1.980(9)
Dy2	O8 ¹	2.402(9)	Dy5	O27	2.297(10)	Cr1	O10	1.980(9)
Dy2	O8	2.403(9)	Dy5	O29	2.372(11)			
Dy2	O35	2.313(14)	Dy5	O31	2.465(9)			
Dy3	O9	2.425(7)	Dy5	O37	2.485(9)			

¹+X,1-Y,+Z; ²-X,1-Y,1-Z

Table S4. Selected Bond Lengths for 1-Y. Related to Figure 1.

Atom	Atom	Length/Å	Atom	Atom	Length/Å	Atom	Atom	Length/Å
Cr1	O8	1.985(6)	Cr3	O31	1.965(7)	Y3	O15	2.301(8)
Cr1	O8 ¹	1.985(6)	Cr3	O32	1.992(7)	Y3	O17	2.448(8)
Cr1	O9	2.007(9)	Y1	O1 ¹	2.390(10)	Y3	O19	2.407(5)
Cr1	O10	1.974(6)	Y1	O1	2.390(10)	Y3	O37	2.479(7)
Cr1	O10 ¹	1.974(6)	Y1	O2	2.391(11)	Y4	O10 ¹	2.376(6)
Cr1	O13	2.006(8)	Y1	O2 ¹	2.391(11)	Y4	O10	2.376(6)
Cr2	N1	2.107(10)	Y1	O3	2.291(12)	Y4	O19	2.276(9)
Cr2	O15	1.927(8)	Y1	O5 ¹	2.357(10)	Y4	O20 ²	2.383(9)
Cr2	O16	1.947(8)	Y1	O5	2.357(10)	Y4	O21 ²	2.566(9)
Y6	O8	2.420(6)	Y1	O35	2.726(11)	Y4	O21	2.298(9)
Y6	O13	2.448(5)	Y1	O36	2.387(16)	Y4	O22 ¹	2.351(7)
Y6	O25	2.691(7)	Y2	O3	2.557(10)	Y4	O22	2.351(7)
Y6	O26	2.486(7)	Y2	O4	2.379(10)	Y5	O12	2.401(7)
Y6	O28	2.308(7)	Y2	O6 ¹	2.332(8)	Y5	O16	2.285(7)
Y6	O31	2.488(7)	Y2	O6	2.332(8)	Y5	O24	2.340(8)
Y6	O33	2.426(7)	Y2	O7	2.288(8)	Y5	O25	2.409(7)
Y6	O34	2.308(7)	Y2	O8 ¹	2.380(6)	Y5	O27	2.272(7)
Cr2	O18	1.998(8)	Y2	O8	2.380(6)	Y5	O29	2.338(8)
Cr2	O23	1.999(9)	Y2	O35	2.270(10)	Y5	O31	2.465(6)
Cr2	O37	1.966(6)	Y3	O9	2.417(5)	Y5	O37	2.463(6)
Cr3	N2	2.088(10)	Y3	O10	2.445(6)	Y6	O7	2.409(5)
Cr3	O27	1.944(7)	Y3	O11	2.474(7)			
Cr3	O28	1.923(7)	Y3	O12	2.653(7)			
Cr3	O30	2.012(8)	Y3	O14	2.307(8)			

¹+X,1-Y,+Z; ²-X,1-Y,1-Z; ³-X,+Y,1-Z

Table S5. ICP-MS measurements for three complexes. Related to Figure 1.

	1-Gd (%)		1-Dy (%)		1-Y (%)	
	Cr	Gd	Cr	Dy	Cr	Y
Calculated	6.80	36.99	6.56	36.92	8.14	25.06
Found	6.79	37.28	6.63	37.37	8.05	25.07

Table S6. The calculated Cr oxidation states.^[a] Related to Figure 1.

1-Gd (BVS)	1-Dy (BVS)	1-Y (BVS)
Cr1 (3.02561)	Cr1 (3.50442)	Cr1 (3.55020)
Cr2 (2.98029)	Cr2 (3.10644)	Cr2 (3.13410)
Cr3 (3.38359)	Cr3 (3.14022)	Cr3 (3.14110)
Gd1 (3.05833)	Dy1 (2.91921)	Y1 (3.16882)
Gd2 (2.94836)	Dy2 (2.90151)	Y2 (3.13556)
Gd3 (3.02187)	Dy3 (2.76503)	Y3 (2.90700)
Gd4 (3.09107)	Dy4 (2.92933)	Y4 (3.06773)
Gd5 (3.06926)	Dy5 (2.83650)	Y5 (3.05496)
Gd6 (3.15810)	Dy6 (2.76173)	Y6 (2.87265)

[a] The bond valence sum was calculated by software EXPO-2014 (<http://www.ba.ic.cnr.it/softwareic/expo/bond-valence-sum/>).

Table S7. The fit parameters of Cole-Cole plots for 1-Dy. Related to Figure 4.

T / K	τ/s	α
1.9	9.778×10^{-5}	0.35813
2.03	8.28227×10^{-5}	0.30576
2.15	6.8656×10^{-5}	0.26042
2.28	4.59675×10^{-5}	0.20784
2.40	3.65471×10^{-5}	0.17701
2.50	2.73006×10^{-5}	0.15741
2.60	1.86163×10^{-5}	0.14874

Supplemental Figures

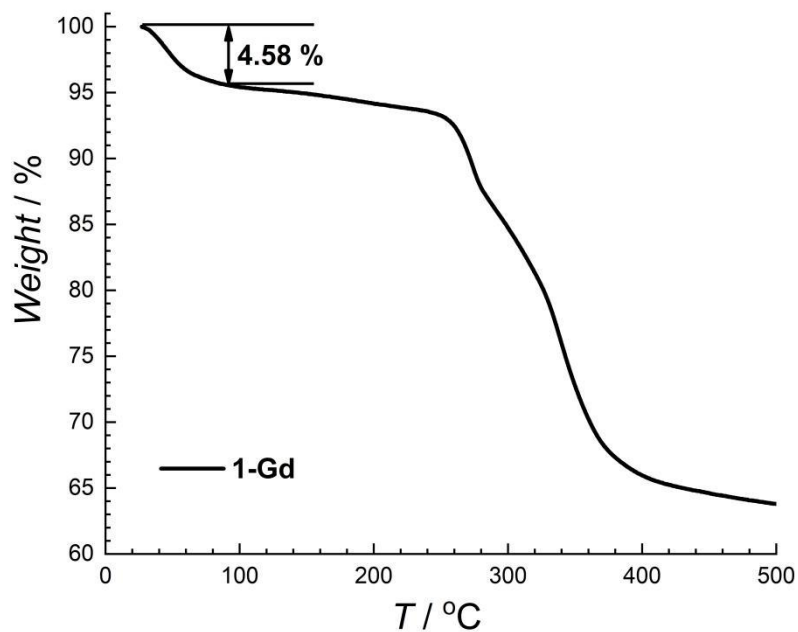


Figure S1. Thermogravimetric analysis (TGA) of 1-Gd. Related to Figure 1.

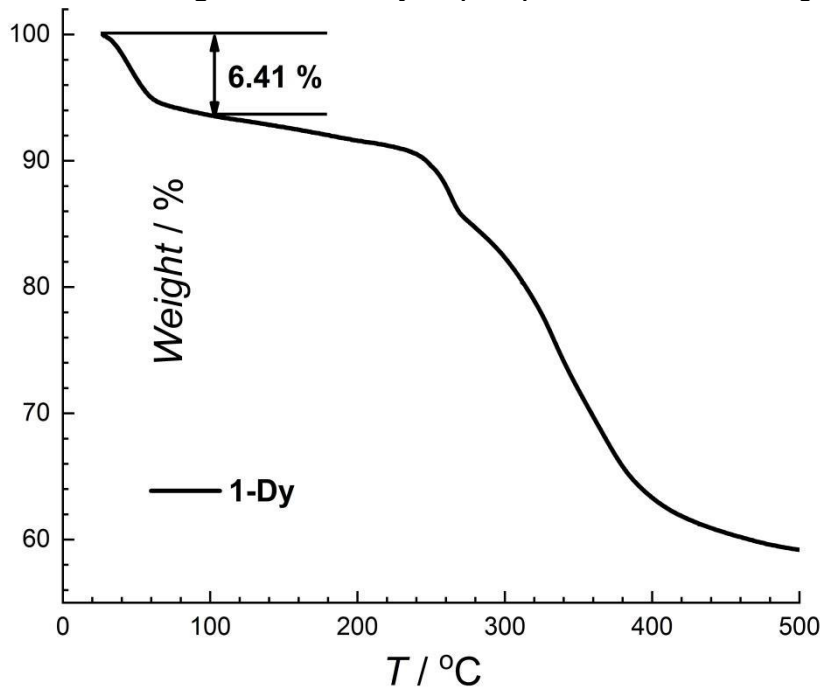


Figure S2. Thermogravimetric analysis (TGA) of 1-Dy. Related to Figure 1.

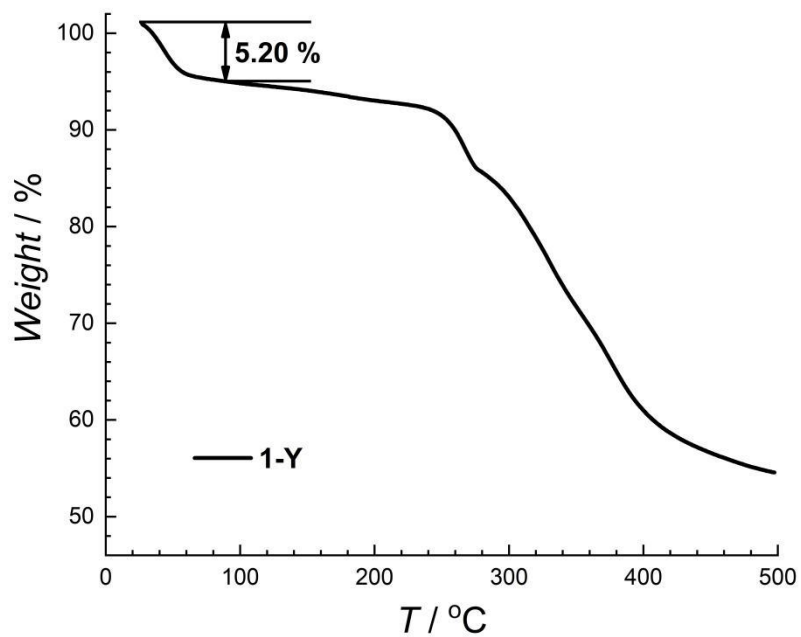


Figure S3. Thermogravimetric analysis (TGA) of 1-Y. Related to Figure 1.

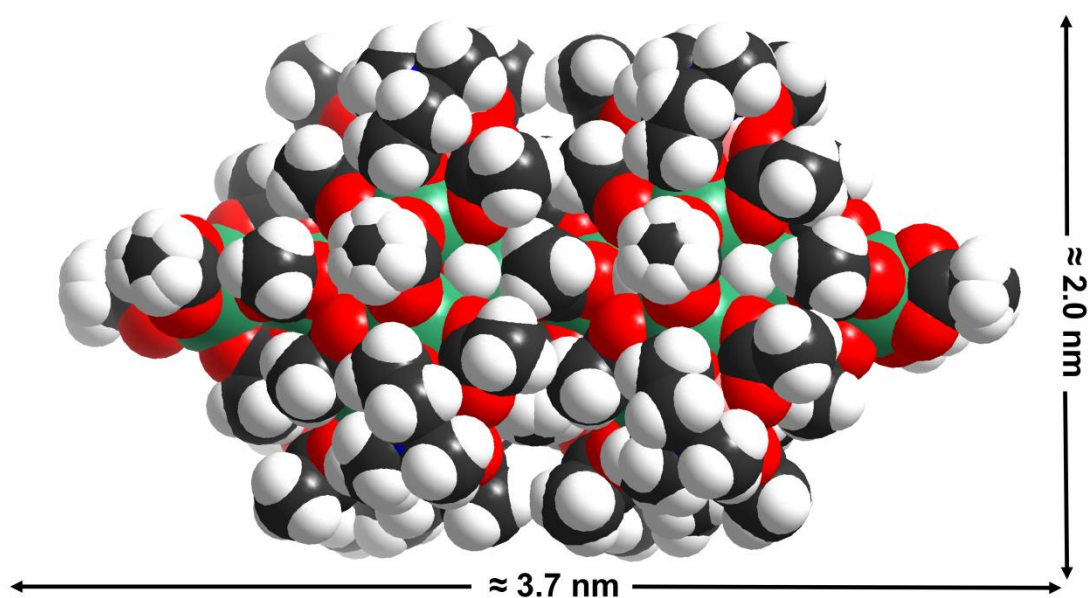


Figure S4. The space-filling model of the complex 1-Gd. Color codes: Cr, pink; Gd, sea green; C, gray; N, blue; O, red.; H, white. Related to Figure 1.

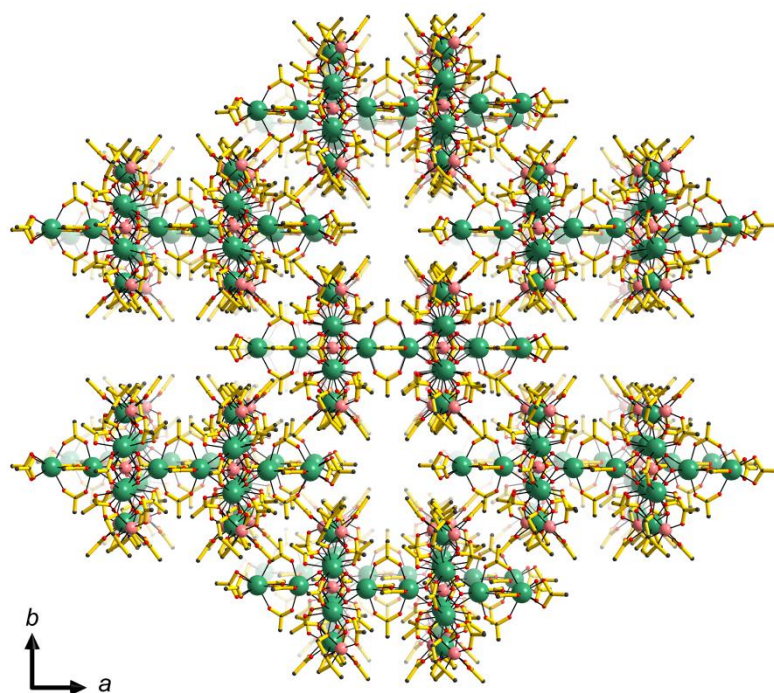


Figure S5. Molecular packing of compound 1-Gd. Color codes: Cr, pink; Gd, sea green; C, gray; N, blue; O, red.; H, white. Related to Figure 1.

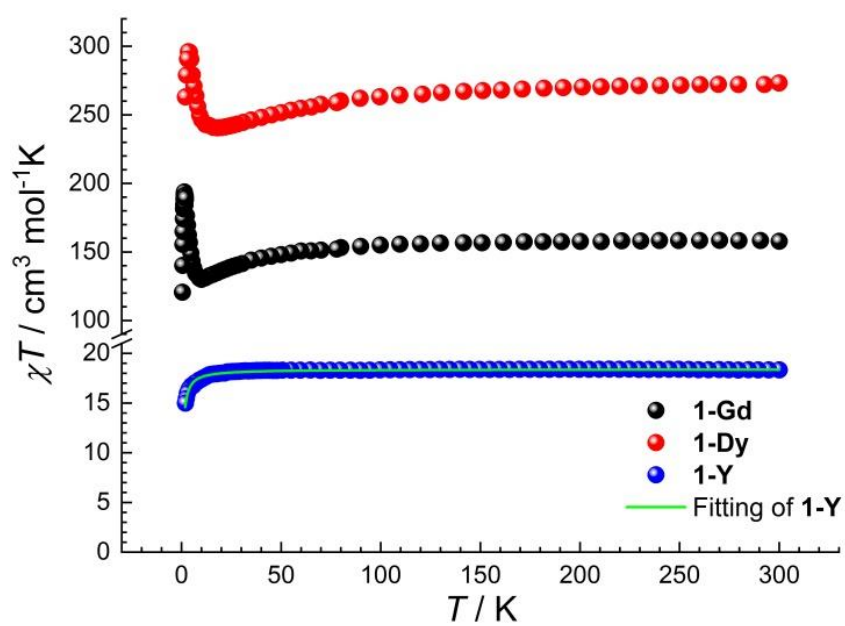


Figure S6. Temperature-dependent dc magnetic susceptibility plots for 1-Gd, 1-Dy, and 1-Y under 1000 Oe, respectively. Related to Figure 2.

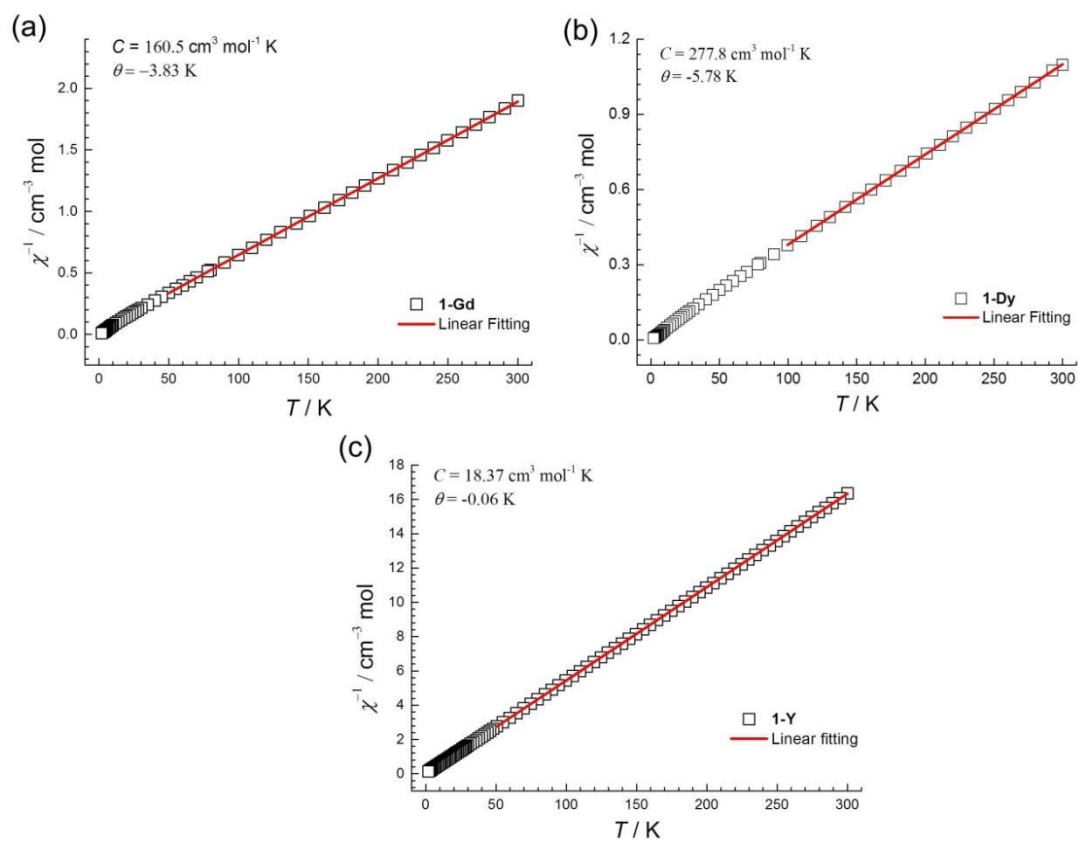


Figure S7. The Curie-Weiss fittings. The Curie-Weiss fittings of the χ^{-1} vs. T plot under 1000 Oe dc field for 1-Gd (a), 1-Dy (b) and 1-Y (c). Related to Figure 2.

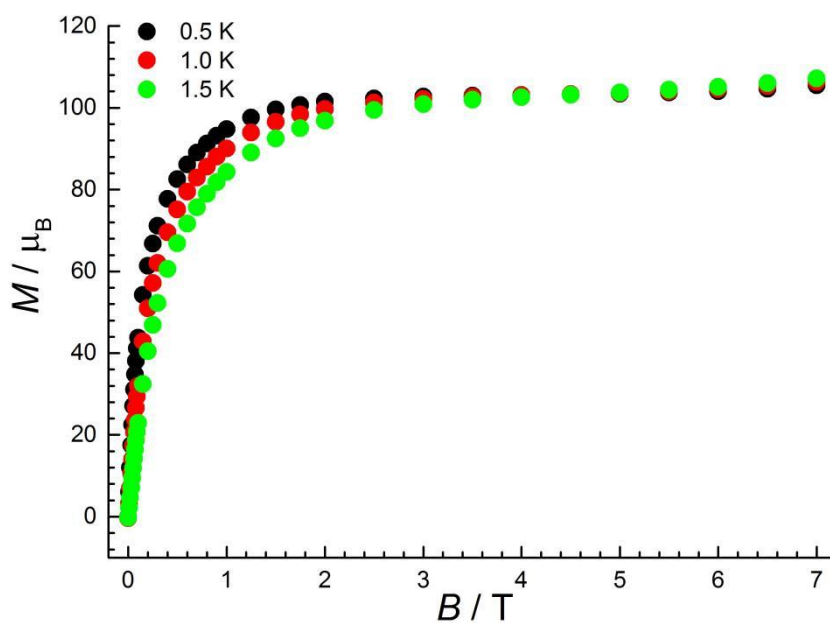


Figure S8. Field-dependent magnetization plots for 1-Gd from 0.5 to 1.5 K. Related to Figure 2 and 3.

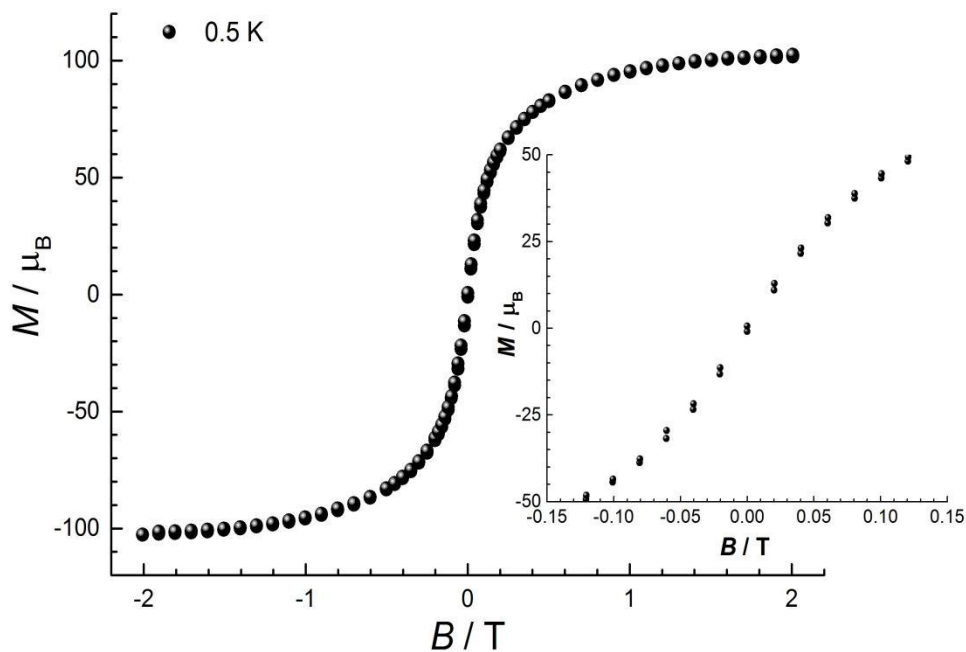


Figure S9. Magnetic hysteresis plots at 0.5 K for 1-Gd with a field sweep rate 6 Oe s^{-1} . The insert is the amplifying part at indicated field range. The lines are guides for the eyes. Related to Figure 2.

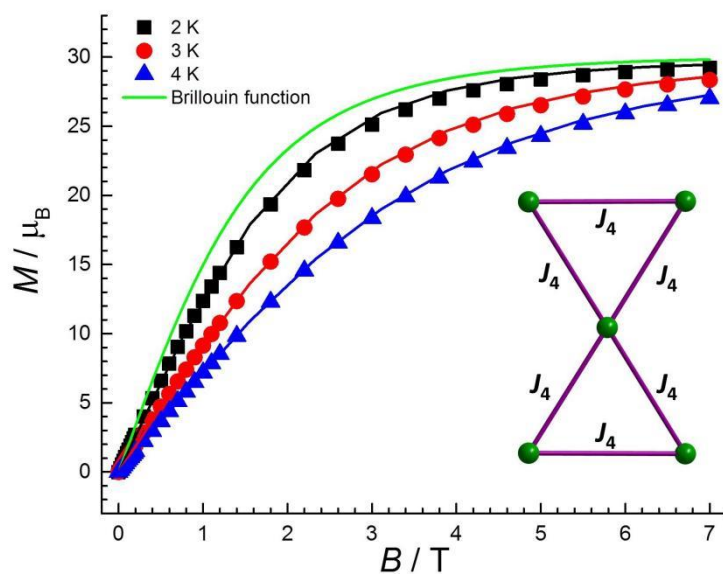


Figure S10. Field-dependent magnetization plots and the fitting results (black, red and blue lines) at indicated temperatures for 1-Y and Brillouin function for ten non-interacting Cr(III) ions at 2 K (solid green line, $g = 2.0$). The insert figure is the fitting $\{\text{Cr}_5\}$ model. Related to Figure 2 and 3.

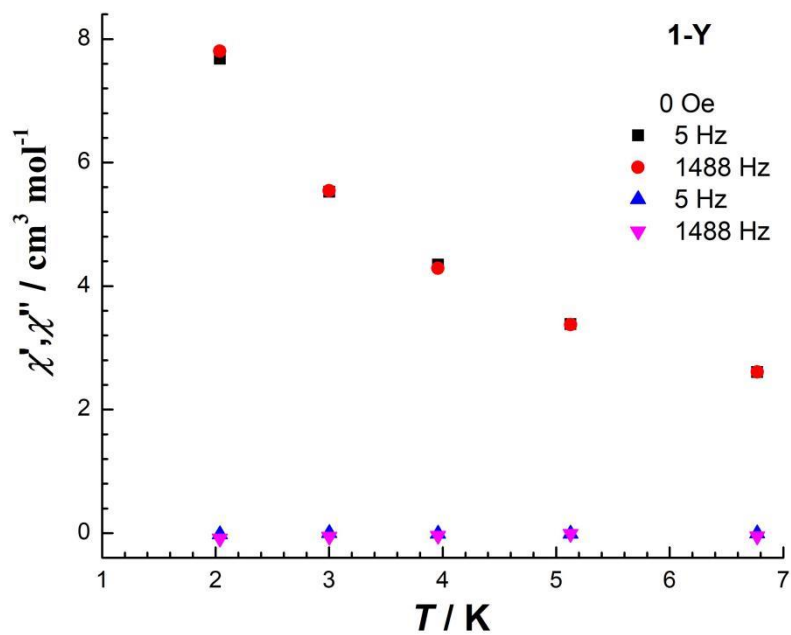


Figure S11. Temperature dependence of the ac susceptibilities for 1-Y at the indicated frequencies under 0 Oe dc field. Related to Figure 2.

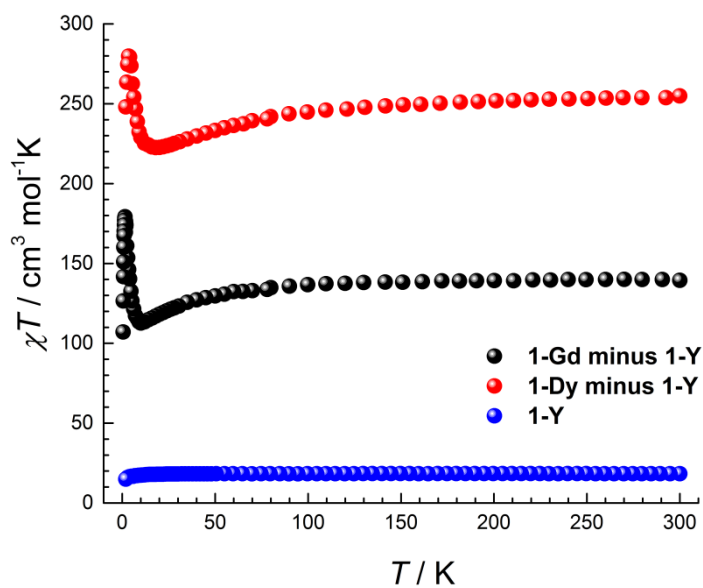


Figure S12. Temperature-dependent dc magnetic susceptibility plots for 1-Gd minus 1-Y data, 1-Dy minus 1-Y data, together with the 1-Y data under 1000 Oe, respectively. Related to Figure 2 and 3.

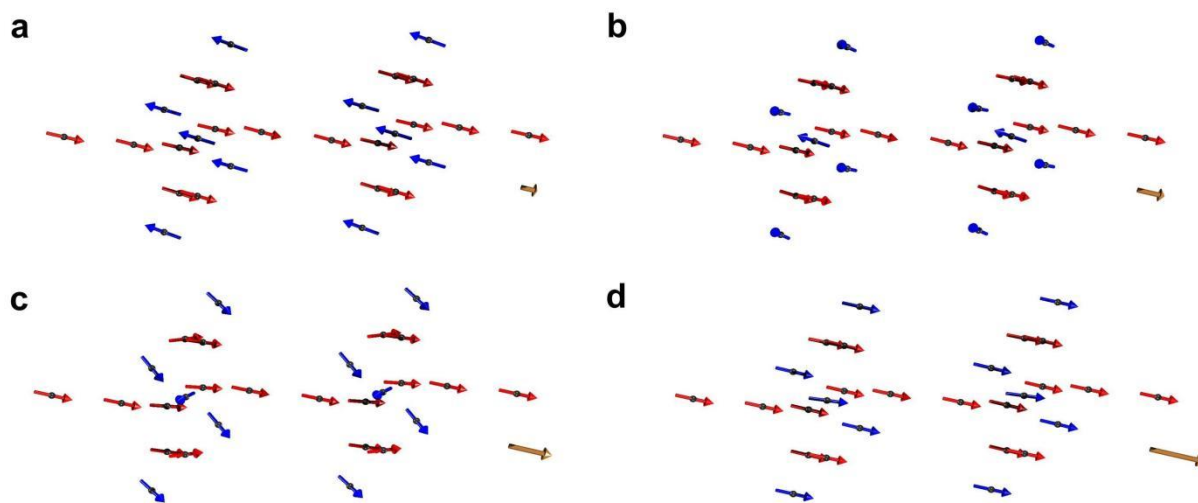


Figure S13. The spin state transitions under low field of 1-Gd. (a) Ferrimagnetic spin configuration ($S = 48$) of our classical model of **1-Gd** in a low magnetic field (displayed as brown arrow in the lower right corner) at $T = 0$. The Cr(III) ions are aligned parallel to the field whereas the Gd(III) ions are aligned antiparallel to the field leading to a stable ferrimagnetic state and hence a constant magnetization plateau, which persists until a certain critical field is reached. (b) Increasing the magnetic field beyond the critical field forces the corner Cr(III) spins to start tilting and rotating towards the field direction. The magnetization starts increasing. (c) Further increasing the magnetic field forces the central Cr(III) spins to start tilting and rotating towards the field direction leading to a further increase of the magnetization. (d) At large enough magnetic field all spins are aligned parallel to the field leading to saturation as observed in our $M(B)$ curve. Related to Figure 3.

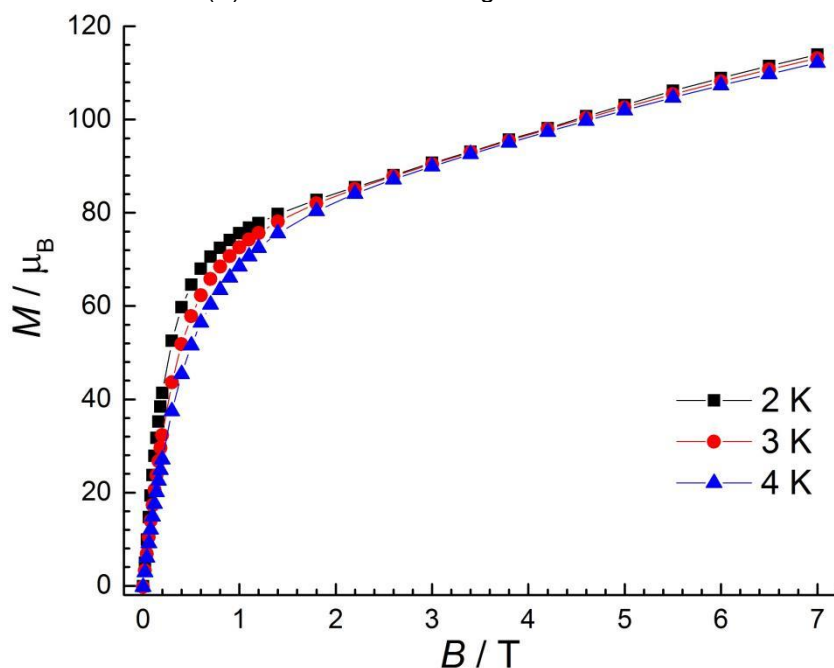


Figure S14. Field-dependent magnetization plots for 1-Dy. Related to Figure 4.

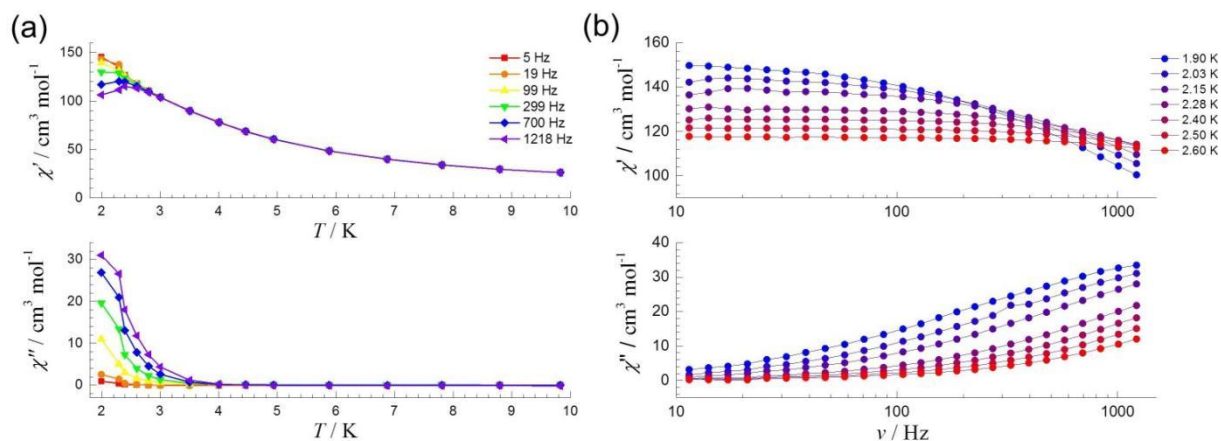


Figure S15. AC magnetic susceptibility for 1-Dy. (a) Temperature (left, the lines are eye guides) and (b) frequency (right, the solid lines are the best fits) ac magnetic susceptibility signals under zero applied dc field with ac field of 3.5 Oe for 1-Dy. Related to Figure 4.

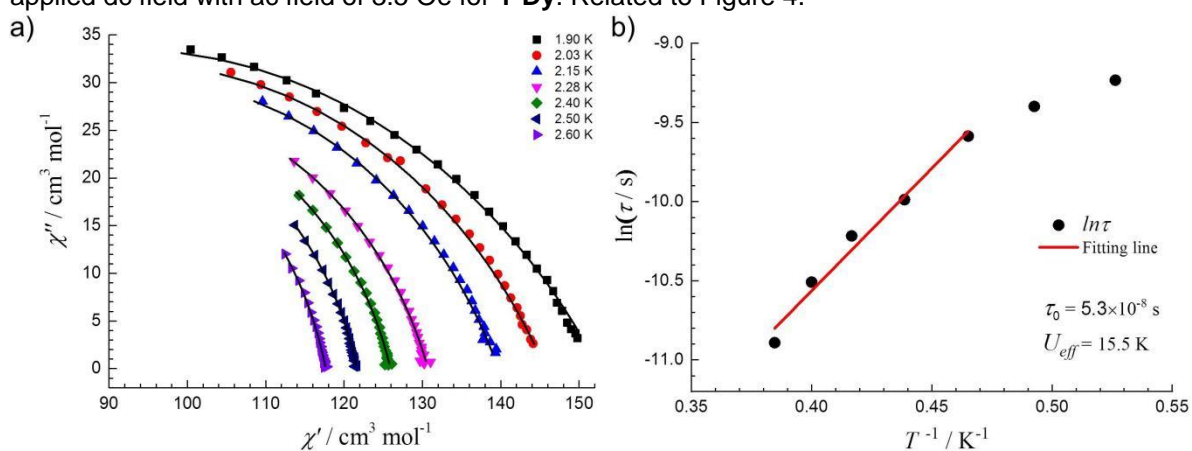


Figure S16. Spin dynamics calculations of 1-Dy under zero field. a) Cole-Cole plots obtained for 1-Dy under zero applied dc field. b) The plots of $\ln(\tau)$ versus $1/T$ for 1-Dy and the linear fitting. Related to Figure 4.

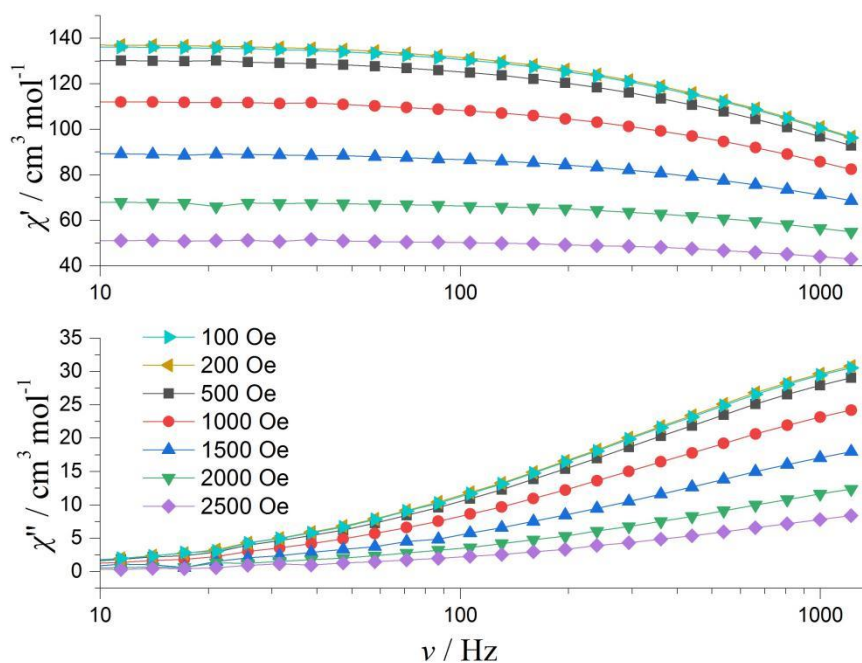


Figure S17. Slow magnetic relaxation behavior of 1-Dy under applied dc field. Frequency-dependent ac magnetic susceptibility signals under indicated dc field with ac field of 3.5 Oe for 1-Dy. Related to Figure 4.

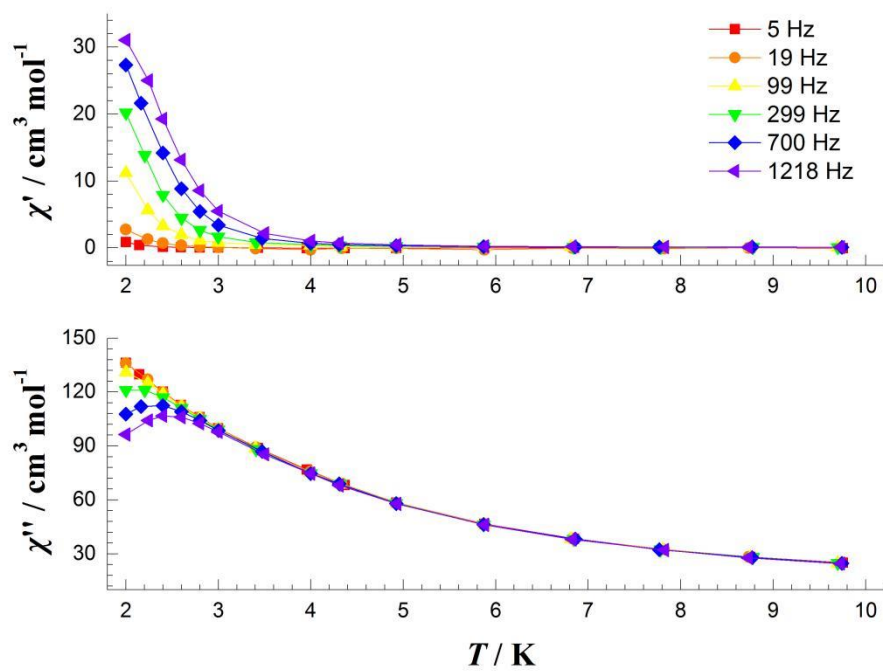
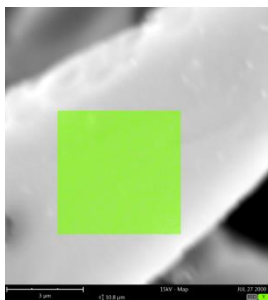


Figure S18. Temperature-dependent ac magnetic susceptibility signals under applied 200 Oe dc field with ac field of 3.5 Oe for 1-Dy. Related to Figure 4.



Element Number	Element Symbol	Element Name	Atomic Conc.	Weight Conc.
39	Y	Yttrium	94.69	90.70
66	Dy	Dysprosium	5.31	9.30

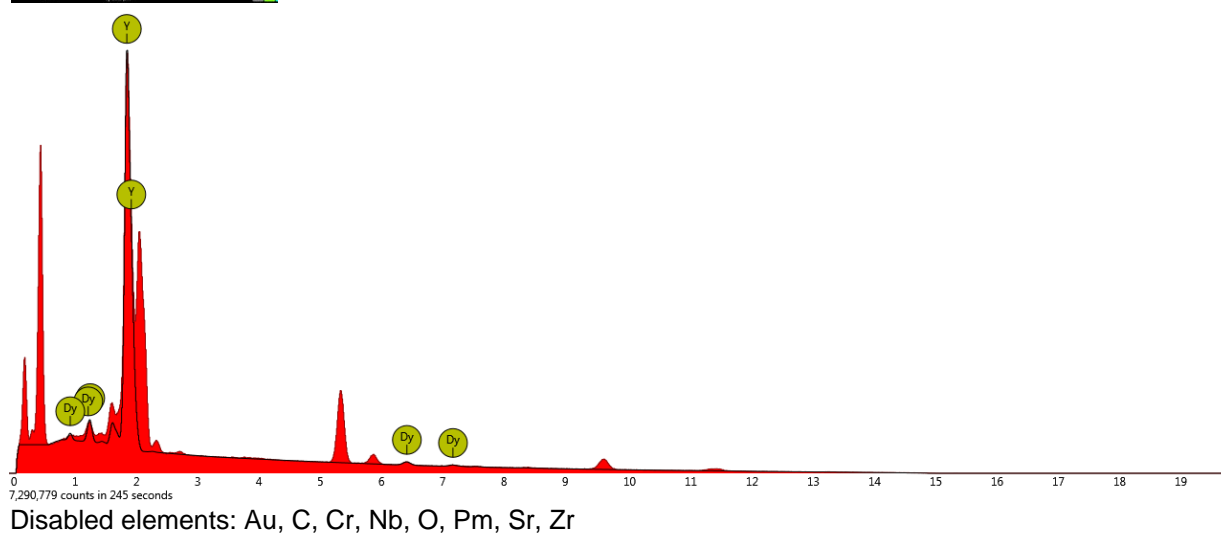


Figure S19. Lanthanide(III) ion content for the magnetic-diluted samples ($1-Y_{0.95}Dy_{0.05}$) determined by energy dispersive spectroscopy (EDS) of field-emission scanning electron microscope. Related to Figure 4.

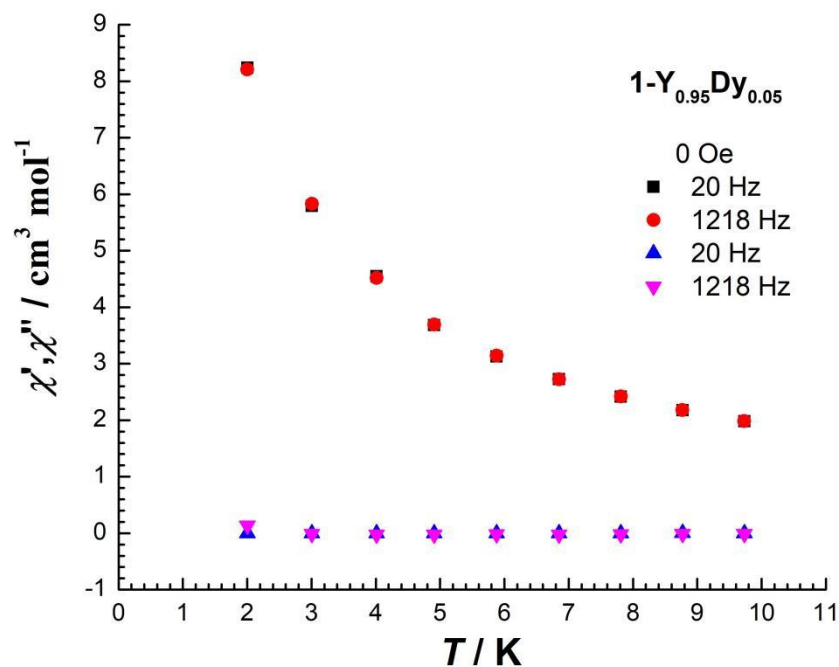


Figure S20. Temperature dependence of the ac susceptibilities for $1-Y_{0.95}Dy_{0.05}$ at the indicated frequencies under 0 Oe dc field. Related to Figure 4.

Transparent Methods

Supplemental Experimental Procedures.

Materials and instrumentation. All reagents and solvents for the syntheses were purchased from commercial sources and used without further purification. Single-crystal X-ray diffraction data were recorded on a Bruker Apex CCD II area-detector diffractometer with graphite-monochromated MoK radiation ($\lambda = 0.71073 \text{ \AA}$) at 298 K for three compounds. Elemental analyses (C, H, and N) were performed on a Vario EL III elemental analyzer. The metal (Cr and RE) contents were analyzed by an inductively coupled plasma mass spectrometry (ICP-MS) instrument (Agilent 7700X). Thermo gravimetric analyses (TGA) were performed with a METTLER TOLEDO TGA2 instrument in an insert Ar atmosphere over a temperature range of 27–500 °C. Magnetic susceptibility and magnetization measurements from 2-300 K were conducted on the Quantum Design MPMS superconducting quantum interference device (SQUID). Ultra-low temperature magnetic susceptibility and magnetization data from 0.5 to 2.0 K were conducted on the MPMS apparatus with an *iHelium-3* accessory with sample inserting in the Ti measuring rod. Infrared spectra (4,000–400 cm^{-1}) of all samples were recorded on a Thermo Scientific Nicolet 6700 FT-IR spectrophotometer. The measurements of the magnetization behaviors under the adiabatic condition at 0.4 K were done by using the pulsed magnetic field, which takes a full cycle. The dysprosium(III) and yttrium(III) contents in **1-Y_{0.95}Dy_{0.05}** sample was investigated using scanning electron microscope (SEM, Su-8010, Hitachi).

Synthesis. All of the three complexes were synthesized in similar synthetic conditions described as follows except for the replacements of $\text{RE}(\text{NO}_3)_3 \cdot 5\text{H}_2\text{O}$ salts. For **1-Gd**, A mixture of $\text{Gd}(\text{NO}_3)_3 \cdot 5\text{H}_2\text{O}$ (433 mg, 1 mmol), $\text{Cr}(\text{acac})_3$ (349 mg, 1 mmol), *N*-methyldiethanolamine (357 mg, 3 mmol), deionized water (0.18 g, 10 mmol), triethylamine (303 mg, 3 mmol) and acetonitrile (8 mL) were sealed in a 12 mL glass vial and then heated at 130 °C with auto-generous pressure. After three days dark green and needle-like crystals were isolated and washed with acetonitrile. Yield: 258 mg, 60.7 % based on Gd. EA analysis (calcd., found): C (21.04, 20.87), H (3.68, 3.32), N (2.01, 2.11). FT-IR (KBr pellets, cm^{-1}): 3700-3050 (br, m), 2868 (w), 1560 (s), 1390 (s), 1338 (m), 1152 (w), 1095 (s), 1022 (m), 1001 (m), 945 (w), 902 (m), 759 (m), 671 (s).

For **1-Dy**, the synthetic condition is similar to **1-Gd**, just using $\text{Dy}(\text{NO}_3)_3 \cdot 5\text{H}_2\text{O}$ (439 mg, 1 mmol) to replace $\text{Gd}(\text{NO}_3)_3 \cdot 5\text{H}_2\text{O}$. Yield: 307 mg, 69.7 % based on Dy. EA analysis (calcd., found): C (21.22, 21.39), H (3.74, 3.55), N (2.48, 2.67). FT-IR (KBr pellets, cm^{-1}): 3700-3040 (br, m), 2865 (w), 1560 (s), 1390 (s), 1337 (m), 1150 (w), 1095 (s), 1021 (m), 1000 (m), 943 (w), 902 (m), 758 (m), 670 (s).

For **1-Y**, the synthetic condition is similar to **1-Gd**, $\text{Y}(\text{NO}_3)_3 \cdot 5\text{H}_2\text{O}$ (365 mg, 1 mmol) to replace $\text{Gd}(\text{NO}_3)_3 \cdot 5\text{H}_2\text{O}$. Yield: 213 mg, 60.0 % based on Y. EA analysis (calcd., found): C (25.21, 25.57), H (4.34, 3.98), N (2.41, 2.30). FT-IR (KBr pellets, cm^{-1}): 3700-3040 (br, m), 2866 (w), 1560 (s), 1390 (s), 1337 (m), 1151 (w), 1095 (s), 1021 (m), 1001 (m), 946 (w), 903 (m), 759 (m), 671 (s).

For **1-Y_{0.95}Dy_{0.05}**, the synthetic condition is similar to **1-Y**, just using the mixture of $\text{Y}(\text{NO}_3)_3 \cdot 5\text{H}_2\text{O}$ (346.8 mg, 0.95 mmol) and $\text{Dy}(\text{NO}_3)_3 \cdot 5\text{H}_2\text{O}$ (21.95 mg, 0.05 mmol) to replace the pure $\text{Y}(\text{NO}_3)_3 \cdot 5\text{H}_2\text{O}$. Yield: 124 mg. EA analysis (calcd., found): C (24.95, 25.23), H (4.37, 4.03), N (2.16, 2.31).

X-ray crystallography. Absorption corrections were applied using the multi-scan technique. Their structures were solved by the direct method of SHELXTL and refined by full-matrix least-square techniques using the SHELXTL program. Severely disordered guest acetonitrile molecules were squeezed by PLATON software. CCDC 1883413-1883415 contain the supplemental crystallographic data for the three complexes in this paper. These data can be obtained free of charge from The Cambridge Crystallographic Data Centre via www.ccdc.cam.ac.uk/data_request/cif.